Machine-learning reveals climate forcing from aerosols is dominated by increased cloud cover

Ying Chen[1*,#], Jim Haywood[1,2], Yu Wang[3], Florent Malavelle[4], George Jordan[2], Daniel Partridge[1], Jonathan Fieldsend[1], Johannes De Leeuw[5], Anja Schmidt[5,6,†], Nayeong Cho[7], Lazaros Oreopoulos[7], Steven Platnick[7], Daniel Grosvenor[8], Paul Field[4,9], Ulrike Lohmann[3]

[1]College of Engineering, Mathematics, and Physical Sciences, University of Exeter, UK
[2]Met Office Hadley Centre, Exeter, UK
[3]Institute for Atmospheric and Climate Science, ETH Zurich, Zurich, Switzerland
[4]Met Office, Exeter, UK
[5]Centre for Atmospheric Science, Yusuf Hamied Department of Chemistry, University of Cambridge, UK
[6]Department of Geography, University of Cambridge, UK
[7]Earth Sciences Division, NASA GSFC, Greenbelt, Maryland, USA
[8]National Centre for Atmospheric Sciences, University of Leeds, Leeds, UK
[9]School of Earth and Environment, University of Leeds, Leeds, UK
[*]Correspondence to: Ying Chen (y.chen6@exeter.ac.uk; ying.chen@psi.ch)
[#]Now at Laboratory of Atmospheric Chemistry, Paul Scherrer Institut, Villigen, Switzerland
[†]Now at Institute of Atmospheric Physics (IPA), German Aerospace Center (DLR), Oberpfaffenhofen, Germany and Meteorological Institute, Ludwig Maximilian University of Munich, Munich, Germany

Abstract:

Aerosol-cloud interactions have a potentially large impact on climate, but are poorly quantified and thus contribute a significant and long-standing uncertainty in climate projections. The impacts derived from climate models are poorly constrained by observations, because retrieving robust large-scale signals of aerosol-cloud interactions are frequently hampered by the considerable noise associated with meteorological co-variability. The Iceland-Holuhraun effusive eruption in 2014 resulted in a massive aerosol plume in an otherwise near-pristine environment and thus provided an ideal natural experiment to quantify cloud responses to aerosol perturbations. Here we disentangle significant signals from the noise of meteorological co-variability using a satellite-based machine-learning approach. Our analysis shows that aerosols from the eruption increased cloud cover by approximately 10%, and this appears to be the leading cause of climate forcing, rather than cloud brightening as previously thought. We find that volcanic aerosols do brighten clouds by reducing droplet size, but this has a significantly smaller radiative impact than changes in cloud fraction. These results add substantial observational constraints on the cooling impact of aerosols. Such constraints are critical for improving climate models, which still inadequately represent the complex macro-physical and micro-physical impacts of aerosol-cloud interactions.

Marine low-level liquid clouds have a profound impact on the energy balance of the Earth system, exerting a net cooling effect by reflecting sunlight[1,2]. It has been previously estimated that only a 6% increase of their albedo could offset the warming from a doubling of CO_2[3,4]. Aerosol-cloud interactions (ACI) are postulated to enhance albedo and prolong the lifetime of liquid clouds[5,6], and therefore counterbalance a substantial, yet poorly constrained, portion of greenhouse gas warming[7-10], leading to only a small net positive overall forcing. As the Earth has warmed by around 1.2 ^{o}C since pre-industrial times[10,11], this would imply that the Earth system is highly sensitive, and therefore vulnerable, to anthropogenic climate forcing[12]. Such a high sensitivity would suggest a very limited remaining carbon budget if the +1.5 ^{o}C target of the 21st Conference of the Parties at Paris (COP21) is to be met[11].

Despite decades of effort, ACI still contribute significantly to uncertainties in climate projections[1,7,9-11]. A primary reason for the large uncertainty in ACI is the lack of suitable large-scale constraints to challenge General Circulation Models (GCMs)[13-15]. ACI operates through processes whereby cloud droplets form on aerosol particles. For a fixed cloud liquid water path (LWP), high concentrations of aerosol lead to more droplets with smaller effective radius (r_{eff}, Twomey r_{eff} effect[5]) which increases cloud albedo. Smaller cloud droplets may inhibit precipitation due to weakened collision-coalescence[6] and suppressed precipitation implies clouds retain more water leading to an increased LWP (LWP adjustment), and prolong their lifetime and areal extent which manifests as increased cloud fraction (CF, CF adjustment)[6]. There is clear evidence of the Twomey r_{eff} effect from numerous comprehensive satellite observations (e.g., ref. [8,15-19]), but continuous debate surrounds the LWP adjustment with different magnitudes and signs reported[8,9,15,20,21], possibly due to confounding adjustments such as effects of entrainment and droplet evaporation processes[22-26]. The CF adjustment is even more difficult to constrain owing to the large-scale impacts of meteorological co-variability[27], leading to long-standing and ongoing disputes in the scientific literature[16,19,28-32]. Satellite

observational constraints of ACI tend to be limited to either small-scale observations or large-scale climatological analyses[33]. A typical example of a small-scale observation is "ship-tracks", manifesting as brighter lines in stratocumulus cloud decks caused by ship emissions. Such small-tracks are generally able to rule out confounding meteorology[8,19], but with a scale far below the resolution of GCMs and a short temporal signature; they are therefore not ideal constraints for these models[33,34]. Climatological analyses examine the correlations between cloud properties and aerosol on a large spatiotemporal scale, but such correlations can be confounded by meteorological co-variability and therefore may not confirm the causal processes of ACI[29,33,35-38].

Here, we overcome these limitations by developing a meteorological reanalysis and satellite-based machine-learning approach that predicts cloud properties in a near-pristine environment, and compare the results with observations of clouds perturbed by the large-scale effusive Icelandic eruption of Holuhraun. The machine-learning approach is enabled by an almost threefold expansion of satellite data from Moderate Resolution Imaging Spectroradiometer (MODIS) compared to the earlier work[15], offering thus a robust training dataset. The machine-learning approach allows us to quantify ACI-induced cloud responses and show an unmistakeable increase in cloud cover. It also allows us to infer the relative contributions to ACI radiative effect from the Twomey effect, and the LWP and CF adjustments. Our results improve current understanding of cloud-induced climate change, and provide robust large-scale constraints for climate models.

Volcanic aerosol perturbation

The effusive volcanic eruption at Holuhraun in Iceland, emitted about 40,000 tonnes of SO_2 per day on average during its eruptive phase in September-October 2014 and 120,000 tonnes

per day at the peak of eruption[15,39]. The sulphate aerosol formed from volcanic SO_2 interacts with liquid-water clouds creating an invaluable natural experiment for testing ACI hypotheses at a large-scale[15]. Detecting CF changes above meteorological noise requires a larger data volume and was left unexplored in the previous study[15], which uses the MODIS Aqua 2002-2014 dataset. Here, by extending the satellite data to both MODIS Aqua and Terra and the length of the analysis period to 2001-2020, we have sufficient training data to develop a robust machine-learning approach for quantitatively disentangling Holuhraun eruption ACI signals from the noise of meteorological co-variability (see Methods). We focus primarily on October 2014, because in this second eruption month the volcanic plume dispersed sufficiently across the entire region of about 3000 km × 6000 km (45^{o}N ~ 75^{o}N; 60^{o}W ~ 30^{o}E, see Supplementary Figure S6.2 in Malavelle et al.[15]). This region is an otherwise near-pristine environment and encompasses the whole spectrum of liquid-dominated cloud regimes, with their frequencies of occurrence being comparable to those observed globally (Extended Data Fig. 1)[15,40].

To disentangle the ACI signal from the noise of meteorological co-variability, we train a machine-learning surrogate MODIS (ML-MODIS) using historical meteorology and MODIS observations during 2001-2020 but excluding the year of the volcanic perturbation (2014, see Methods). ML-MODIS is designed to predict cloud properties for given meteorological conditions when unperturbed by volcanic aerosol. Our "leave-one-year-out" cross validation (see Methods) shows that the surrogate ML-MODIS can reproduce the MODIS observations of cloud droplet number concentration (N_d), r_{eff}, LWP and CF when no volcanic aerosol-perturbation exists, as shown in the left column of Fig. 1. However, significant differences between the ML-MODIS predictions and MODIS observations are observed in the presence of the volcanic perturbation in October 2014 (right column of Fig. 1). Similar results are found for September 2014 (Supplementary Discussion section S1).

We examine the ACI corresponding to the increase in N_d instead of aerosol optical depth, because MODIS aerosol products are hampered by the overcast nature of the geographical region and using N_d has several advantages as a mediating variable[29]. We first quantify the increase in N_d and then estimate the susceptibility of other cloud properties, i.e., $dlnr_{eff}/dlnN_d$, $dlnLWP/dlnN_d$, and $dlnCF/dlnN_d$. The volcano-induced increase in N_d is observed across nearly the entire region with a positive signal across the zonal means (Fig. 2a). We also observe a clear shift of the N_d probability distribution towards larger values due to the volcanic perturbation with an average increase of 20 cm^{-3}.

We perform Monte Carlo analyses (see Methods) to estimate the uncertainty of ML-MODIS and to quantify the impact of ACI on relevant cloud properties. In assessing the statistical uncertainties, we follow the Intergovernmental Panel on Climate Change (IPCC) uncertainty guideline[41] and use the 90% probabilities (that are assigned "very likely"). A validation of ML-MODIS by MODIS for conditions unperturbed by Holuhraun is further achieved by these results, with median and average values close to the 1:1 line (Fig. 3) and with a 90% probability of the Pearson correlation coefficients (R) exceeding 0.6 for N_d, r_{eff} and CF (Extended Data Fig. 2, higher than 0.5 for LWP). In contrast, the 90% probability of R being below 0.6 for all cloud properties in volcano-perturbed conditions, indicates large influences of the volcanic aerosol on cloud properties. We estimate a volcanic aerosol-induced increase in N_d of 28% over the region (Fig. 3, showing that the ratio between ML-MODIS and MODIS is 1.27 with against 0.99 without volcano), which is clearly statistically significant because the perturbation lies outside the range of uncertainty of the machine-learning method. This increase is similar to the ~32% increase in N_d from pre-industrial to present day according to multi-model estimates[14], suggesting that the results from our analysis may be a reasonable proxy for anthropogenic aerosols in terms of the strength in perturbing clouds since pre-industrial times.

Twomey effect and liquid water path adjustment

We first use our machine-learning approach to examine the Twomey r_{eff} effect and LWP adjustment. We observe a consistent spatial pattern of volcano-induced increase in N_d and an average reduction in r_{eff} (Figs. 2a and 2b) from 15.2 μm to 13.9 μm. The spatial pattern is also consistent with the climatological MODIS anomaly analysis[15] (Extended Data Fig. 3), but with some difference in the strength of ACI signal. This further demonstrates the viability of our machine-learning approach in identifying changes in cloud created by volcanic aerosols above those expected due to meteorological variability. Climatological anomalies may identify regions influenced by the Holuhraun plume[15] but may not be robust in quantifying ACI signals arising from Holuhraun, because the ACI signal is confounded by meteorology where 2014 conditions are not necessarily equal to climatological average. Indeed, while Malavelle et al.[15] developed a robust method for removing the meteorological variability in the modelled response, they also cautioned that meteorological differences from the long-term mean could cause some of the observed response (their Figures S6.1 and S6.2). Our machine-learning approach overcomes these issues (Methods, see also Supplementary Discussion section S1 and S2). We estimate an 8% decrease in r_{eff} as a response to a 28% increase in N_d on average (and median) over the geographical region (Fig. 3). In line with previous studies[8,17,31], no significant LWP response is found when examining the region as a whole (Fig. 3 and Extended Data Fig. 4). This may be due to the cancellation of the LWP adjustment-induced increase[6] by entrainment-induced decrease of LWP[22], as suggested by Toll et al.[8] who examined over 10,000 globally representative aerosol-perturbation tracks of small-scale in liquid clouds.

Cloud fraction response

So far results from our large-scale machine-learning approach agree with previous analyses: a distinct and robust Twomey r_{eff} effect but a weak LWP adjustment (e.g., ref. [8,17,31]). We now examine the adjustment of liquid phase CF, which is a macro-property of cloud and difficult to examine using small-scale aerosol-induced tracks[8]. Our results of volcanic aerosol-perturbed conditions show an overall increase of zonal CF at all latitudes of our domain, and a clear shift of probability distribution from a median value of 0.36 to 0.39 (Fig. 2c). The CF increase exhibits a spatial pattern that is consistent with the Twomey r_{eff} effect (Fig. 2b and 2c). This strongly suggests that it is the aerosol perturbation that leads to increased cloud cover, since the Twomey r_{eff} effect has been well documented as an ACI indicator[8,9,15,18].

We present the response of CF and other cloud properties over the geographical region using the Monte Carlo method (Fig. 3). For all non-perturbed cloud properties, the validation shows the median and average values on the 1:1 line. For volcano-induced changes in N_d and r_{eff}, we confirm the expected increase and decrease respectively, but see little LWP response. For CF, we observe a statistically significant median (and average) relative increase of 11% with the signal variability range lying outside the uncertainty. We estimate $d\ln CF/d\ln N_d = 0.41$ [0.05 ~ 1.53, 90% confidence interval], indicating a strong susceptibility of CF to aerosol-induced perturbation in N_d. Rosenfeld et al.[30] found a similar strong susceptibility using a climatological approach, but for the convective cores of southern ocean liquid clouds. This strong susceptibility is also consistent with other studies (e.g. ref. [16,29,31,36]), although, unlike the present study, their results are likely either influenced by the confounding meteorology associated with the climatological correlation approach[33,36] or limited by relatively small-scale Lagrangian trajectories[33]. For example, Ghan et al.[14] showed that climatological correlation analysis differs greatly from perturbation analysis across multiple GCMs, despite efforts to classify and isolate different meteorological regimes.

To back up our finding of CF increase, we perform a traditional climatological anomaly analysis which shows a similar spatial pattern for the CF response (Extended Data Fig. 3c). Additionally, we investigate the impact of the unusually low sea-surface temperature that developed to the south of the region (Extended Data Fig. 5a) owing to factors that appear to be independent from the eruption[42]. While this could affect CF, it cannot be accounted for in the climatological anomaly analysis using only MODIS data. Our machine-learning approach, however, accounts for this variability (Extended Data Fig. 6 and Supplementary Discussion section S2). We are therefore in position to better quantify a significantly weaker CF increase over the corresponding region (45^{o}N ~ 60^{o}N, 20^{o}W ~ 45^{o}W; compare Fig. 2c against Extended Data Fig. 3c). We also find 14% fewer cloud-free high-resolution (1-km^2) MODIS pixels during October 2014 compared to the long-term October mean. Again, this implies CF increases in response to the volcanic aerosol. Any conceivable increase in cloud cover from ice-clouds is also investigated and cannot be discerned (Extended Data Fig. 5b); this suggests that any potential confounding effect from ice-cloud or transition to ice-cloud is small, and that our results regarding ACI of liquid clouds are robust.

Cloud fraction adjustment dominates radiative forcing

We revisit the relative contributions to ACI-induced radiative forcing from the Twomey effect, LWP and CF adjustments, see Methods section "Radiative Forcing". In line with previous studies[8,31], we find a weak contribution (2 ± 17%) from the LWP adjustment. However, in contrast to recent studies reporting that the Twomey r_{eff} effect dominates (> 70%) the ACI radiative forcing[8,19,31]; we show that, for this large-scale study across a wide range of meteorological and cloud regimes, the CF adjustment (61 ± 23%) surpasses the Twomey r_{eff} effect (37 ± 18%) in terms of ACI cooling (Fig. 3). This new finding may be due to the much

larger spatiotemporal scales of our investigation, which extends up to tens of thousands of km with perturbation lasting for months. Given the large range of meteorological conditions and cloud regimes included (Extended Data Fig. 1), our study appears arguably more suitable for constraining large-scale climate models and ACI associated with anthropogenic emissions, which themselves persist across many geographical areas and are associated with a wide variety of cloud regimes.

Our results suggest that cooling caused by a CF increase is substantially underestimated in current climate projections[10]. A recent multi-model assessment of the susceptibility of $dlnCF/dlnN_d$ versus $-dlnr_{eff}/dlnN_d$ (Ghan et al.[14]; their Figure 1) suggests ratios of approximately 1:3. Our results suggest that the CF adjustment is possibly larger than the Twomey r_{eff} effect, since the ratio of their susceptibilities is around 5:4. It is possible that GCMs compensate for the lack of CF response with overly strong LWP adjustment[8,10,15,19,34] – i.e. estimate the "right" cooling but for manifestly the wrong reasons.

This work sheds light into certain aspects of ACI which conventionally thought to follow the following route: an increase in aerosols gives rise to i) an increase in N_d leading to ii) a larger number of smaller cloud droplets leading to iii) a decrease in the collision-coalescence growth rate of cloud droplets, leading to iv) a reduction in precipitation leading to v) an increase in LWP leading to vi) an increase in cloud lifetime leading to vii) an increase in CF. Malavelle et al.[15] suggested that iv) and v) do not operate as expected, while, this new study provides strong evidence for vi) and vii). This conundrum needs to be addressed in further research. Suggestions for how to approach this in future work includes performing large eddy model simulation of the Holuhraun event to identify difference in the ACI causal chain between the heavily parameterized GCMs representation and the more explicit cloud-resolving models. Identifying any changes in cloud regimes (e.g., ref. [31,40]) might also provide further clues in

solving this puzzle. We maintain that because clouds are such a fundamentally important component of the Earth's hydrological cycle and energy flows that the underlying reasons of deficient model performance need to be urgently addressed. Our findings appear to provide robust new constraints for climate models, despite the uncertainties associated with machine-learning and MODIS retrievals. We acknowledge that the cold SST anomaly in October 2014 could potentially introduce more uncertainty in the machine-learning representation of cloud conditions, but this influence appears insignificant in this study (Supplementary Discussion Section S2). ACI signals are statistically significant, lying outside the uncertainty range of the machine-learning approach (Fig. 3). Uncertainty in the MODIS retrievals can be decomposed into systematic errors and random errors. Random errors are greatly suppressed by averaging over a geographical region of thousands of kilometres[43], while systematic errors are largely cancelled when taking differences between MODIS and ML-MODIS[8].

The quantified constraints from our machine-learning study pave the way to advance our current understanding of physical ACI processes, and point to new directions and challenges towards future improvement of climate models. With advances in both areas, we expect that our large-scale constraints on ACI will lead to reduced uncertainty in climate projections and future estimates of climate sensitivity.

Acknowledgments

We would like to acknowledge the support of the UK Natural Environment Research Council (NERC) funded ADVANCE project (NE/T006897/1) which funded JH, YC, DP, AS, DG and PF. JH, GJ and FM were also part funded under funding provided by the EU's Horizon 2020 research and innovation programme under the CONSTRAIN grant agreement 820829. JH, PF, GJ, AJ and FM are supported by the Joint UK BEIS/Defra Met Office Hadley Centre Climate Programme (GA01101). YW would like to thank the support from Mr. Philippe Sarasin and the ETH Zurich Foundation (ETH Fellowship project: 2021-HS-332). DG is funded by the National Centre for Atmospheric Science (NCAS), one of the UK NERC's research centres. JdL acknowledges funding from the NERC funded V-PLUS grant NE/S00436X/1. NC, LO and SEP are funded by USA NASA programs. The machine-learning training is performed using the "Statistics and Machine Learning Toolbox" in MATLAB (version R2019b, MathWorks Inc., Natick, MA, USA). We would like to thank Ken Carslaw (University of Leeds) for co-developing and co-leading the Leeds aspect of ADVANCE project, and Andy Jones (UK Met Office) for helpful discussions.

Author contributions Statement

YC and JH conceived the study. YW and YC designed and developed the machine-learning approach used in this study with help from JH and JF. JH led the ADVANCE project funded by UK-NERC. YC, FM, JG and JH performed the analysis of MODIS data with help from DG, NC, LO and SEP. NC, LO and SEP performed the cloud regime analysis. YC, JH, YW, DG, UL, PF, LO, SEP, JdL, AS, DP and JF contributed to the uncertainty discussion. YC and JH performed the analyses and interpreted the results with inputs from all co-authors. YC and JH led the manuscript writing with specific inputs and edits from DG, LO and UL. All co-authors discussed the results and commented on the manuscript.

Competing Interests Statement: The authors declare no competing interests.

Figure Legends/Captions:

Fig. 1 | Comparison between machine-learning predictions (ML-MODIS) and MODIS observations. Left panels (a-d): validation against non-perturbed observations (excluding 2014) of cloud properties, from top to bottom they show cloud droplet number concentration (N_d), cloud droplet effective radius (r_{eff}), cloud liquid water path (LWP) and cloud fraction (CF). Right panels (e-h): volcanic perturbation signals in October 2014, indicated by the difference between the machine-learning predictions and the observations. October MODIS observations from Aqua (2002-2020) and Terra (2001-2020) are analyzed. Colour indicates the normalized data density function with a maximum value of one, with 80% of the data being contained within the black dashed area.

Fig. 2 | Changes in cloud properties caused by the volcanic perturbation estimated using machine-learning predictions and MODIS observations for October 2014**.** The spatial distribution and zonal means of the changes in N_d, r_{eff} and CF are shown in the left panels of **a-c** while right panels show probability density functions (so that the areas under the curves are equivalent) for MODIS and ML-MODIS.

Fig. 3 | Responses of cloud properties to the volcanic aerosol-perturbation in October 2014. The aerosol-cloud interactions (ACI) signals of responses are indicated as the ratios between MODIS (Aqua and Terra) observations and machine-learning predictions, i.e., Ratio = MODIS divided by ML-MODIS. Uncertainties of non-perturbed baseline references are estimated using a Monte Carlo method and are shown in black (see Methods, based on non-volcanic October datasets spanning 2001-2020). The variability of the cloud responses to the Holuhraun volcanic aerosol perturbation are shown in pink. The boxplots show 10^{th}, 25^{th}, median (Med.), 75^{th} and 90^{th} percentiles with the mean value indicated by a dot. The susceptibilities of r_{eff}, LWP and CF to changes in N_d are given in a green colour, median [90% confidence interval]. Area (in units of km^2) weighted averaging is used to calculate average cloud properties over the geographical region (Fig. 2), in order to estimate an unbiased large-scale response signal. Therefore, the ratios shown here are slightly different from the slopes shown in Fig. 1, in which area-weighted averaging is not applied.

References:

1 Lohmann, U. & Feichter, J. Global indirect aerosol effects: a review. *Atmos. Chem. Phys.* **5**, 715-737, doi:10.5194/acp-5-715-2005 (2005).

2 L'Ecuyer, T. S., Hang, Y., Matus, A. V. & Wang, Z. Reassessing the Effect of Cloud Type on Earth's Energy Balance in the Age of Active Spaceborne Observations. Part I: Top of Atmosphere and Surface. *Journal of Climate* **32**, 6197-6217, doi:10.1175/jcli-d-18-0753.1 (2019).

3 Latham, J. *et al.* Global temperature stabilization via controlled albedo enhancement of low-level maritime clouds. *Philosophical Transactions of the Royal Society A: Mathematical, Physical and Engineering Sciences* **366**, 3969-3987, doi:doi:10.1098/rsta.2008.0137 (2008).

4 Chen, Y.-C., Christensen, M. W., Stephens, G. L. & Seinfeld, J. H. Satellite-based estimate of global aerosol–cloud radiative forcing by marine warm clouds. *Nature Geoscience* **7**, 643-646, doi:10.1038/ngeo2214 (2014).

5 Twomey, S. Pollution and the planetary albedo. *Atmospheric Environment* **8**, 1251-1256, doi:https://doi.org/10.1016/0004-6981(74)90004-3 (1974).

6 Albrecht, B. A. Aerosols, Cloud Microphysics, and Fractional Cloudiness. *Science* **245**, 1227-1230, doi:10.1126/science.245.4923.1227 (1989).

7 Boucher, O. *et al.* in *Climate Change 2013: The Physical Science Basis. Contribution of Working Group I to the Fifth Assessment Report of the Intergovernmental Panel on Climate Change* (eds T. F. Stocker *et al.*) 571-657 (Cambridge University Press, 2013).

8 Toll, V., Christensen, M., Quaas, J. & Bellouin, N. Weak average liquid-cloud-water response to anthropogenic aerosols. *Nature* **572**, 51-55, doi:10.1038/s41586-019-1423-9 (2019).

9 Bellouin, N. *et al.* Bounding Global Aerosol Radiative Forcing of Climate Change. *Reviews of Geophysics* **58**, e2019RG000660, doi:10.1029/2019rg000660 (2020).

10 IPCC. Climate Change 2021: The Physical Science Basis. Contribution of Working Group I to the Sixth Assessment Report of the Intergovernmental Panel on Climate Change [Masson-Delmotte, V., P. Zhai, A. Pirani, S.L. Connors, C. Péan, S. Berger, N. Caud, Y. Chen, L. Goldfarb, M.I. Gomis, M. Huang, K. Leitzell, E. Lonnoy, J.B.R. Matthews, T.K. Maycock, T. Waterfield, O. Yelekçi, R. Yu, and B. Zhou (eds.)]. *Cambridge University Press* **In Press** (2021).

11 Rogelj, J., Forster, P. M., Kriegler, E., Smith, C. J. & Séférian, R. Estimating and tracking the remaining carbon budget for stringent climate targets. *Nature* **571**, 335-342, doi:10.1038/s41586-019-1368-z (2019).

12 Andreae, M. O., Jones, C. D. & Cox, P. M. Strong present-day aerosol cooling implies a hot future. *Nature* **435**, 1187-1190 (2005).

13 Seinfeld, J. H. *et al.* Improving our fundamental understanding of the role of aerosol−cloud interactions in the climate system. *Proceedings of the National Academy of Sciences* **113**, 5781-5790, doi:10.1073/pnas.1514043113 (2016).

14 Ghan, S. *et al.* Challenges in constraining anthropogenic aerosol effects on cloud radiative forcing using present-day spatiotemporal variability. *Proceedings of the National Academy of Sciences* **113**, 5804-5811, doi:10.1073/pnas.1514036113 (2016).

15 Malavelle, F. F. *et al.* Strong constraints on aerosol–cloud interactions from volcanic eruptions. *Nature* **546**, 485-491, doi:10.1038/nature22974 (2017).

16 Kaufman, Y. J., Koren, I., Remer, L. A., Rosenfeld, D. & Rudich, Y. The effect of smoke, dust, and pollution aerosol on shallow cloud development over the Atlantic Ocean. *Proceedings of the National Academy of Sciences of the United States of America* **102**, 11207-11212, doi:10.1073/pnas.0505191102 (2005).

17 McCoy, D. T. & Hartmann, D. L. Observations of a substantial cloud-aerosol indirect effect during the 2014–2015 Bárðarbunga-Veiðivötn fissure eruption in Iceland. *Geophysical Research Letters* **42**, 10,409-410,414, doi:https://doi.org/10.1002/2015GL067070 (2015).

18 Toll, V., Christensen, M., Gassó, S. & Bellouin, N. Volcano and Ship Tracks Indicate Excessive Aerosol-Induced Cloud Water Increases in a Climate Model. *Geophysical Research Letters* **44**, 12,492-412,500, doi:10.1002/2017gl075280 (2017).

19 Diamond, M. S., Director, H. M., Eastman, R., Possner, A. & Wood, R. Substantial Cloud Brightening From Shipping in Subtropical Low Clouds. *AGU Advances* **1**, e2019AV000111, doi:https://doi.org/10.1029/2019AV000111 (2020).
20 Gryspeerdt, E. *et al.* Constraining the aerosol influence on cloud liquid water path. *Atmos. Chem. Phys.* **19**, 5331-5347, doi:10.5194/acp-19-5331-2019 (2019).
21 Possner, A., Eastman, R., Bender, F. & Glassmeier, F. Deconvolution of boundary layer depth and aerosol constraints on cloud water path in subtropical stratocumulus decks. *Atmos. Chem. Phys.* **20**, 3609-3621, doi:10.5194/acp-20-3609-2020 (2020).
22 Ackerman, A. S., Kirkpatrick, M. P., Stevens, D. E. & Toon, O. B. The impact of humidity above stratiform clouds on indirect aerosol climate forcing. *Nature* **432**, 1014-1017, doi:10.1038/nature03174 (2004).
23 Stevens, B. & Feingold, G. Untangling aerosol effects on clouds and precipitation in a buffered system. *Nature* **461**, 607-613, doi:10.1038/nature08281 (2009).
24 Lebo, Z. J. & Feingold, G. On the relationship between responses in cloud water and precipitation to changes in aerosol. *Atmos. Chem. Phys.* **14**, 11817-11831, doi:10.5194/acp-14-11817-2014 (2014).
25 Koren, I., Dagan, G. & Altaratz, O. From aerosol-limited to invigoration of warm convective clouds. *Science* **344**, 1143-1146, doi:10.1126/science.1252595 (2014).
26 Seifert, A., Heus, T., Pincus, R. & Stevens, B. Large-eddy simulation of the transient and near-equilibrium behavior of precipitating shallow convection. *Journal of Advances in Modeling Earth Systems* **7**, 1918-1937, doi:https://doi.org/10.1002/2015MS000489 (2015).
27 Mauger, G. S. & Norris, J. R. Meteorological bias in satellite estimates of aerosol-cloud relationships. *Geophysical Research Letters* **34**, doi:https://doi.org/10.1029/2007GL029952 (2007).
28 Kaufman, Y. J. & Koren, I. Smoke and Pollution Aerosol Effect on Cloud Cover. *Science* **313**, 655-658, doi:10.1126/science.1126232 (2006).
29 Gryspeerdt, E., Quaas, J. & Bellouin, N. Constraining the aerosol influence on cloud fraction. *Journal of Geophysical Research: Atmospheres* **121**, 3566-3583, doi:https://doi.org/10.1002/2015JD023744 (2016).
30 Rosenfeld, D. *et al.* Aerosol-driven droplet concentrations dominate coverage and water of oceanic low-level clouds. *Science* **363**, eaav0566, doi:10.1126/science.aav0566 (2019).
31 Christensen, M. W., Jones, W. K. & Stier, P. Aerosols enhance cloud lifetime and brightness along the stratus-to-cumulus transition. *Proceedings of the National Academy of Sciences* **117**, 17591-17598, doi:10.1073/pnas.1921231117 (2020).
32 Breen, K. H., Barahona, D., Yuan, T., Bian, H. & James, S. C. Effect of volcanic emissions on clouds during the 2008 and 2018 Kilauea degassing events. *Atmos. Chem. Phys.* **21**, 7749-7771, doi:10.5194/acp-21-7749-2021 (2021).
33 Glassmeier, F. *et al.* Aerosol-cloud-climate cooling overestimated by ship-track data. *Science* **371**, 485-489, doi:10.1126/science.abd3980 (2021).
34 Christensen, M. W. *et al.* Opportunistic experiments to constrain aerosol effective radiative forcing. *Atmos. Chem. Phys.* **22**, 641-674, doi:10.5194/acp-22-641-2022 (2022).
35 Bender, F. A. M., Frey, L., McCoy, D. T., Grosvenor, D. P. & Mohrmann, J. K. Assessment of aerosol–cloud–radiation correlations in satellite observations, climate models and reanalysis. *Climate Dynamics* **52**, 4371-4392, doi:10.1007/s00382-018-4384-z (2019).
36 Fuchs, J., Cermak, J. & Andersen, H. Building a cloud in the southeast Atlantic: understanding low-cloud controls based on satellite observations with machine learning. *Atmos. Chem. Phys.* **18**, 16537-16552, doi:10.5194/acp-18-16537-2018 (2018).
37 Oreopoulos, L., Cho, N. & Lee, D. A Global Survey of Apparent Aerosol-Cloud Interaction Signals. *Journal of Geophysical Research: Atmospheres* **125**, e2019JD031287, doi:https://doi.org/10.1029/2019JD031287 (2020).
38 Fan, J., Wang, Y., Rosenfeld, D. & Liu, X. Review of Aerosol–Cloud Interactions: Mechanisms, Significance, and Challenges. *Journal of the Atmospheric Sciences* **73**, 4221-4252, doi:10.1175/jas-d-16-0037.1 (2016).
39 Gettelman, A., Schmidt, A. & Egill Kristjánsson, J. Icelandic volcanic emissions and climate. *Nature Geoscience* **8**, 243-243, doi:10.1038/ngeo2376 (2015).

40 Oreopoulos, L., Cho, N., Lee, D. & Kato, S. Radiative effects of global MODIS cloud regimes. *Journal of Geophysical Research: Atmospheres* **121**, 2299-2317, doi:https://doi.org/10.1002/2015JD024502 (2016).

41 IPCC. Guidance Note for Lead Authors of the IPCC Fifth Assessment Report on Consistent Treatment of Uncertainties. https://www.ipcc.ch/site/assets/uploads/2017/2008/AR2015_Uncertainty_Guidance_Note.pdf (2010).

42 Grist, J. P. *et al.* Extreme air–sea interaction over the North Atlantic subpolar gyre during the winter of 2013–2014 and its sub-surface legacy. *Climate Dynamics* **46**, 4027-4045, doi:10.1007/s00382-015-2819-3 (2016).

43 Grosvenor, D. P. *et al.* Remote Sensing of Droplet Number Concentration in Warm Clouds: A Review of the Current State of Knowledge and Perspectives. *Reviews of Geophysics* **56**, 409-453, doi:https://doi.org/10.1029/2017RG000593 (2018).

Methods

MODIS observations

We used the Level-3 products of MODIS Collection 6.1, i.e., MYD08 for 2002-2020 from Aqua and MOD08 for 2001-2020 from Terra. The reported retrieval bias due to instrument degradation in Terra-MODIS Collection 5.1 datasets[15] has been rectified in Collection 6.1. An inadvertent artifact in the calculations of cloud fraction (derived from cloud optical property) in Collection 5.1 has also been removed in Collection 6.1[44] and both Terra-MODIS and Aqua-MODIS now show consistent results[45,46]. Cloud droplet effective radius (r_{eff}), in-cloud liquid water path (LWP), cloud optical thickness and cloud phase are retrieved from observed radiances using a radiative transfer model at 1-km nadir resolution in Level-2 products and aggregated to the $1^o \times 1^o$ Level-3 products[46]. The Level-3 Cloud Optical Property Cloud Fraction product for the liquid phase (dataset name Cloud Retrieval Fraction Liquid)[46] is used in the cloud fraction (CF) analysis, because this CF product can distinguish between clouds of liquid and ice phase and is consistent with the other microphysical retrievals of cloud properties used in this study. Note that ref. [17] used MODIS Collection 6 data, and used cloud fraction derived from the cloud mask[47] multiplied by the fractional liquid cloud and found a more modest increase in cloud fraction of ~1.7% in October. Differences between our findings and those from ref. [17] in the climatological analysis likely arise from a combination of the use of different CF products, the extension of the MODIS data to include data from 2015-2020, and differences in the areas of investigation. Monthly-mean products are used in this study, with differences being negligible when aggregating Level-3 daily products into monthly means[15,32]. An exception is liquid cloud droplet number concentration (N_d) which is derived from r_{eff} and cloud optical thickness assuming adiabatic conditions[8,20,31,48], and because of non-linear dependences, N_d is first obtained daily and then averaged to monthly means[48,49]. Only pixels with r_{eff} between 4 μm to 30 μm and cloud optical thickness between 4 to 70 are used for the

most reliable N_d retrievals[49]. The uncertainty of the derived N_d is discussed in detail in Grosvenor et al.[43] who estimated that the uncertainty can be largely reduced to about 50% when averaged over $1^o \times 1^o$ regions. The uncertainty is expected to be even smaller in our study, since we average across a geographical region of about 3000 km × 6000 km.

To further back up our finding of increased CF, we also analysed the frequency of cloud-free conditions in arguably the most stringent MODIS product, namely pixels with retrieved aerosol optical depth (AOD) at 550 nm which are used as a proxy of cloud-free pixels. This pixels are most stringent because any thin or sub-grid scale cloud is screened out to prevent contamination of AOD retrievals. Level-3 monthly MODIS AOD products record the number of validated 1-km^2 pixels used in the Level-2 products when performing aggregation. These statistics are used to calculate the relative reduction of cloud-free pixels in our region in October 2014 relative to the long-term 2001-2020 October mean excluding 2014. While the number of pixels with AOD retrievals do not have a one-to-one correspondence to the number of cloud-free pixels because factors such as sun-glint in cloud-free pixels can reduce the number of AOD pixels, it is still a good relative (rather than absolute) proxy for cloud-free pixels.

Meteorological reanalyses

Meteorological reanalyses represent the best estimate of global atmospheric conditions[50], and are available from the European Centre for Medium-Range Weather Forecasts ERA5 products (https://cds.climate.copernicus.eu/). To train the machine-learning surrogate MODIS (ML-MODIS), we use the monthly averaged ERA5 reanalysis from the surface up to 550 hPa level at $0.25^o \times 0.25^o$ horizontal resolution and 50 hPa vertical resolution. This vertical range covers most of the low-level liquid clouds. In total, 114 meteorological parameters are re-gridded to MODIS grid cells and used in the training, details of which are provided in Supplementary Table S1. The ERA5 monthly reanalysis products at 11:00 and 13:00 Icelandic time (same as

UTC) are closest to the daytime Terra and Aqua overpass times and are paired with the respective MODIS products from these satellites for the training.

Machine-learning

Previous studies that use machine-learning to investigate the statistical correlation between cloud properties and aerosol (e.g., ref. [36,51]) can possibly be affected by confounding meteorological co-variability that would prevent confirmation of the causal processes of aerosol-cloud interactions (ACI)[33,36]. Here, we use a random forest algorithm[52] to train a ML-MODIS that diagnoses cloud properties for given meteorological conditions but unperturbed by volcanic aerosol. This allows comparisons of cloud properties between conditions with and without volcanic aerosol-perturbation but otherwise alike, therefore quantifying cloud responses only to volcanic aerosol, i.e. signals of ACI. Note that this machine-learning approach is not designed to calculate the temporal evolution of cloud properties and cannot predict the development of meteorological systems. The latter is obtained from the ERA5 reanalysis, which provides the best estimate of atmospheric state[50].

The random forest algorithm is chosen because of its excellent performance in dealing with relatively small sample sizes and high-dimensional feature spaces and in avoiding over-fitting[52,53]. Random forest based machine-learning has been successfully applied to isolate the confounding meteorological variability in air quality assessments and has been shown to perform much better than multinomial regression models[54-56]. A regression mode forest of one hundred trees is trained independently for each cloud property (N_d, r_{eff}, LWP and CF) and for each month (October and September), with a minimal leaf size of seven for each tree without merge leaves. Each tree samples ~60% of the input data with replacement for the training data and the remaining data is used as out-of-bag observations. With larger forests, we find a negligible reduction in out-of-bag mean squared error and a negligible increase in out-of-bag

coefficient of determination (a more informative estimate of performance than mean squared error[57]) of up to 0.87 for CF prediction. This indicates a good stability and avoidance of over-fitting[58]. The number of randomly selected predictors is 38 (one third of the total number of features) and the interactive-curvature method is used to select split predictors. The ERA5 meteorological reanalysis is independent of the MODIS datasets, which are not assimilated in the reanalysis[50], and provides the explanatory variables in the ML-MODIS training. The dependent variables are the corresponding cloud properties observed by MODIS with no volcanic eruption. The successful training of ML-MODIS is enabled by the large MODIS dataset from continuous observations over the past 20 years on two satellite platforms. We employ the "out-of-bag permuted predictor delta error" method[52,59] to measure the importance of each explanatory feature in predicting cloud properties. The results for CF shown in Extended Data Fig. 6.

The performance of ML-MODIS as a surrogate of the MODIS observations under conditions without the volcanic perturbation is evaluated using "leave-one-year-out" cross validation[60] for each cloud property, as shown in the left panels of Fig. 1 and Extended Data Fig. 7. This involves training ML-MODIS using randomly selected sets of 18 years of ERA5-MODIS dataset pairs and then evaluating ML-MODIS against the remaining 19th year of MODIS observations. This evaluation is carried out for each non-eruption year during 2001-2020. The uncertainty of ML-MODIS is further estimated using a Monte Carlo method, and the variability of the reference baselines are shown as black boxplots in Fig. 3 and Extended Data Fig. 8a. For the Monte Carlo uncertainty estimate, we randomly perform "leave-one-year-out" validation 500 times for each cloud property, by excluding both Terra and Aqua datasets of the randomly selected year over the entire region from machine-learning training but use them for validation. A test for N_d using the validation of a 700-member Monte Carlo ensemble showed negligible differences. The ratios of cloud properties between the ML-MODIS prediction (without

volcano-perturbation) and MODIS observations in 2014 (with volcano-perturbation) are in pink in Fig. 3 for October and in Extended Data Fig. 8a for September, with the pink boxplots showing the variability of all decision-trees within the random forest Monte Carlo ensembles, i.e., the variability of the ACI signals.

Radiative forcing

We estimate the relative contributions from the Twomey r_{eff}, LWP adjustment, and CF adjustment to ACI-induced radiative forcing using the susceptibilities of r_{eff}, LWP and CF to N_d perturbations. The radiative forcing arising from cloud albedo brightening can be described as Eq. (1) at a constant CF[8,9,61], and the forcing arising from CF enhancement can be described as Eq. (2) at a constant cloud albedo α_{cld}.

$$\left.\frac{dSW_{TOA}}{d\ln AOD}\right|_{CF} = -SW_{down} \times CF \times \alpha_{cld} \times (1-\alpha_{cld}) \times \frac{d\ln N_d}{d\ln AOD} \times (\frac{1}{3} + \frac{5}{6}\frac{d\ln LWP}{d\ln N_d}) \quad \textbf{(1)}$$

$$\left.\frac{dSW_{TOA}}{d\ln AOD}\right|_{albedo} = -SW_{down} \times (\alpha_{cld} - \alpha_{cs}) \times \frac{dCF}{d\ln AOD} = -SW_{down} \times (\alpha_{cld} - \alpha_{cs}) \times CF \times \frac{d\ln CF}{d\ln N_d} \times \frac{d\ln N_d}{d\ln AOD} \quad \textbf{(2)}$$

where $d\mathrm{SW}_{\mathrm{TOA}}$ is the short-wave radiative forcing at the top of atmosphere, $\mathrm{SW}_{\mathrm{down}}$ is the incoming short-wave solar radiation at the top of the atmosphere, α_{cld} is the average broadband short-wave cloud albedo with a global mean of 0.38 for liquid clouds[9], and α_{cs} is clear-sky broadband ocean surface albedo which is about 0.07 for representative of global average (solar zenith angle of 60 degrees)[62]. The total ACI-induced short-wave radiative forcing is the sum of Eq. (1) and Eq. (2), as shown in Eq. (3).

$$\begin{aligned}\frac{dSW_{TOA}}{d\ln AOD} &= \left.\frac{dSW_{TOA}}{d\ln AOD}\right|_{albedo} + \left.\frac{dSW_{TOA}}{d\ln AOD}\right|_{CF} \\ &= -SW_{down} \times CF \times \frac{d\ln N_d}{d\ln AOD} \times [\frac{1}{3}\alpha_{cld}(1-\alpha_{cld}) + \alpha_{cld}(1-\alpha_{cld}) \times \frac{5}{6}\frac{d\ln LWP}{d\ln N_d} + (\alpha_{cld} - \alpha_{cs})\frac{d\ln CF}{d\ln N_d}]\end{aligned} \quad \textbf{(3)}$$

The radiative forcing contributions from the Twomey r_{eff} effect, LWP adjustment and CF adjustment are described as the three terms in the square bracket from left to right, respectively.

Data availability: The MODIS cloud and aerosol products from Aqua (MYD08_L3) and Terra (MOD08_L3) used in this study are available from the Atmosphere Archive and Distribution System Distributed Active Archive Center of National Aeronautics and Space Administration (LAADS-DAAC, NASA), https://ladsweb.modaps.eosdis.nasa.gov. ERA5 datasets are available from the European Centre for Medium-range Weather Forecast (ECMWF) archive, https://cds.climate.copernicus.eu. The full datasets shown in the figures are provided in source data files.

Code availability: Code is available from the corresponding author on reasonable request.

References for Methods and Supplementary Information:

44 Platnick, A. S. *et al.* MODIS Cloud Optical Properties: User Guide for the Collection 6/6.1 Level-2 MOD06/MYD06 Product and Associated Level-3 Datasets. *https://atmosphere-imager.gsfc.nasa.gov/sites/default/files/ModAtmo/MODISCloudOpticalPropertyUserGuideFinal_v1.1_1.pdf* (2018).

45 Platnick, S. *et al.* The MODIS Cloud Optical and Microphysical Products: Collection 6 Updates and Examples From Terra and Aqua. *IEEE Transactions on Geoscience and Remote Sensing* **55**, 502-525, doi:10.1109/TGRS.2016.2610522 (2017).

46 Hubanks, P., Platnick, A. S., King, M. & Ridgway, B. MODIS Atmosphere L3 Gridded Product Algorithm Theoretical Basis Document (ATBD) & Users Guide. *available from: https://icdc.cen.uni-hamburg.de/fileadmin/user_upload/icdc_Dokumente/MODIS/MODIS_Collection6_AtmosphereL3_GriddedProduct_ATBDandUsersGuide_v4.1_Sep22_2015.pdf* (2019).

47 Maddux, B. C., Ackerman, S. A. & Platnick, S. Viewing Geometry Dependencies in MODIS Cloud Products. *Journal of Atmospheric and Oceanic Technology* **27**, 1519-1528, doi:10.1175/2010jtecha1432.1 (2010).

48 Quaas, J., Boucher, O., Bellouin, N. & Kinne, S. Satellite-based estimate of the direct and indirect aerosol climate forcing. *Journal of Geophysical Research: Atmospheres* **113**, doi:https://doi.org/10.1029/2007JD008962 (2008).

49 Quaas, J., Boucher, O. & Lohmann, U. Constraining the total aerosol indirect effect in the LMDZ and ECHAM4 GCMs using MODIS satellite data. *Atmos. Chem. Phys.* **6**, 947-955, doi:10.5194/acp-6-947-2006 (2006).

50 Hersbach, H. *et al.* The ERA5 global reanalysis. *Quarterly Journal of the Royal Meteorological Society* **146**, 1999-2049, doi:https://doi.org/10.1002/qj.3803 (2020).

51 Andersen, H., Cermak, J., Fuchs, J., Knutti, R. & Lohmann, U. Understanding the drivers of marine liquid-water cloud occurrence and properties with global observations using neural networks. *Atmos. Chem. Phys.* **17**, 9535-9546, doi:10.5194/acp-17-9535-2017 (2017).

52 Breiman, L. Random Forests. *Machine Learning* **45**, 5-32, doi:10.1023/A:1010933404324 (2001).

53 Biau, G. & Scornet, E. A random forest guided tour. *TEST* **25**, 197-227, doi:10.1007/s11749-016-0481-7 (2016).

54 Grange, S. K., Carslaw, D. C., Lewis, A. C., Boleti, E. & Hueglin, C. Random forest meteorological normalisation models for Swiss PM10 trend analysis. *Atmos. Chem. Phys.* **18**, 6223-6239, doi:10.5194/acp-18-6223-2018 (2018).
55 Shi, Z. *et al.* Abrupt but smaller than expected changes in surface air quality attributable to COVID-19 lockdowns. *Science Advances* **7**, eabd6696, doi:10.1126/sciadv.abd6696 (2021).
56 Yang, J. *et al.* From COVID-19 to future electrification: Assessing traffic impacts on air quality by a machine-learning model. *Proceedings of the National Academy of Sciences* **118**, e2102705118, doi:10.1073/pnas.2102705118 (2021).
57 Chicco, D., Warrens, M. J. & Jurman, G. The coefficient of determination R-squared is more informative than SMAPE, MAE, MAPE, MSE and RMSE in regression analysis evaluation. *PeerJ Computer Science* **7**, e623, doi:10.7717/peerj-cs.623 (2021).
58 Cutler, A., Cutler, D. R. & Stevens, J. R. Random Forests. In: Zhang C., Ma Y. (eds) Ensemble Machine Learning. . *Springer, Boston, MA.* , doi:https://doi.org/10.1007/978-1-4419-9326-7_5 (2012).
59 Bonte, S., Goethals, I. & Holen, R. V. in *2017 IEEE Nuclear Science Symposium and Medical Imaging Conference (NSS/MIC).* 1-3.
60 Bastos, L. S. & O'Hagan, A. Diagnostics for Gaussian Process Emulators. *Technometrics* **51**, 425-438, doi:10.1198/TECH.2009.08019 (2009).
61 Ackerman, A. S. *et al.* Effects of Aerosols on Cloud Albedo: Evaluation of Twomey's Parameterization of Cloud Susceptibility Using Measurements of Ship Tracks. *Journal of the Atmospheric Sciences* **57**, 2684-2695, doi:10.1175/1520-0469(2000)057<2684:eoaoca>2.0.co;2 (2000).
62 Jin, Z., Charlock, T. P., Smith Jr., W. L. & Rutledge, K. A parameterization of ocean surface albedo. *Geophysical Research Letters* **31**, doi:https://doi.org/10.1029/2004GL021180 (2004).
63 Twigg, M. M. *et al.* Impacts of the 2014–2015 Holuhraun eruption on the UK atmosphere. *Atmos. Chem. Phys.* **16**, 11415-11431, doi:10.5194/acp-16-11415-2016 (2016).
64 Myers, T. A. & Norris, J. R. On the Relationships between Subtropical Clouds and Meteorology in Observations and CMIP3 and CMIP5 Models. *Journal of Climate* **28**, 2945-2967, doi:10.1175/jcli-d-14-00475.1 (2015).
65 Höjgård-Olsen, E. *Observations of the tropical atmospheric water cycle and its variations with sea surface temperature using a constellation of satellites Observations du cycle de l'eau atmosphérique tropicale et de ses variations avec la température de surface de la mer, à l'aide d'une constellation de satellites*, Université Paris-Saclay, (2020).
66 Costa, A. A., Cotton, W. R., Walko, R. L., Pielke, R. A. & Jiang, H. SST Sensitivities in Multiday TOGA COARE Cloud-Resolving Simulations. *Journal of the Atmospheric Sciences* **58**, 253-268, doi:10.1175/1520-0469(2001)058<0253:Ssimtc>2.0.Co;2 (2001).
67 Sandu, I., Stevens, B. & Pincus, R. On the transitions in marine boundary layer cloudiness. *Atmos. Chem. Phys.* **10**, 2377-2391, doi:10.5194/acp-10-2377-2010 (2010).

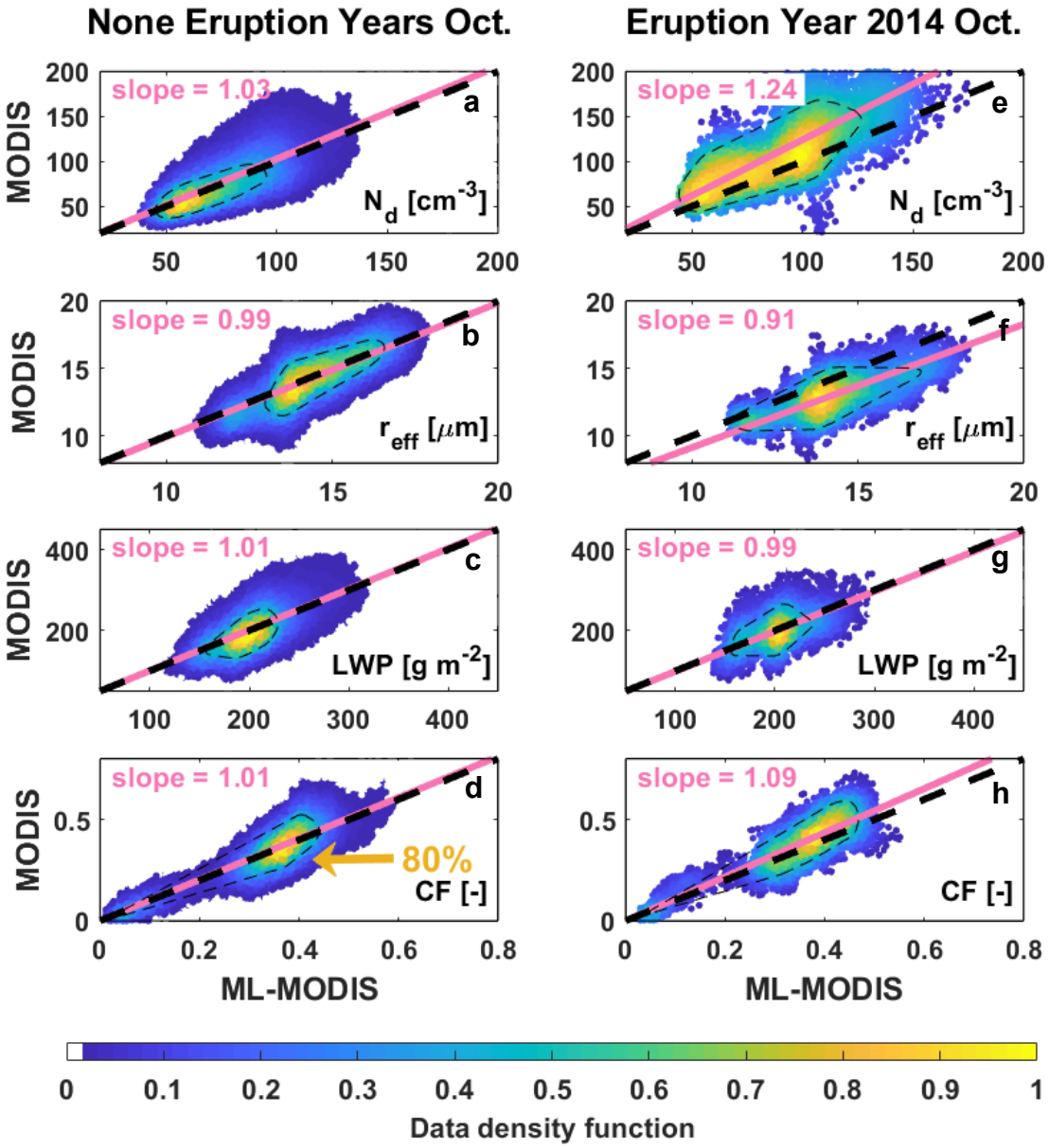

Fig. 1 | Comparison between machine-learning predictions (ML-MODIS) and MODIS observations. Left panels (a-d): validation against non-perturbed observations (excluding 2014) of cloud properties, from top to bottom they show cloud droplet number concentration (N_d), cloud droplet effective radius (r_{eff}), cloud liquid water path (LWP) and cloud fraction (CF). Right panels (e-h): volcanic perturbation signals in October 2014, indicated by the difference between the machine-learning predictions and the observations. October MODIS observations from Aqua (2002-2020) and Terra (2001-2020) are analyzed. Colour indicates the normalized data density function with a maximum value of one, with 80% of the data being contained within the black dashed area.

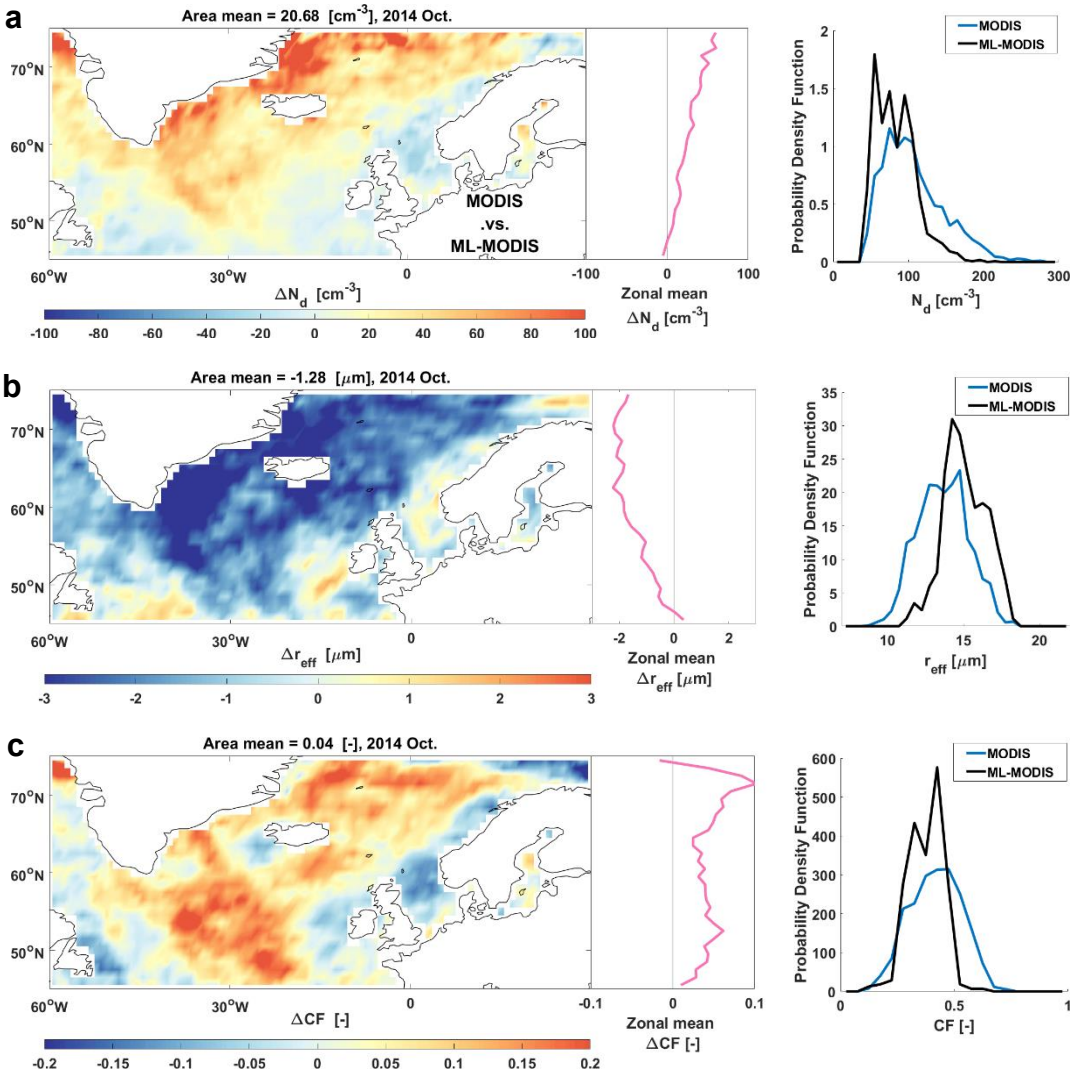

Fig. 2 | Changes in cloud properties caused by the volcanic perturbation estimated using machine-learning predictions and MODIS observations for October 2014**.** The spatial distribution and zonal means of the changes in N_d, r_{eff} and CF are shown in the left panels of **a-c** while right panels show probability density functions (so that the areas under the curves are equivalent) for MODIS and ML-MODIS.

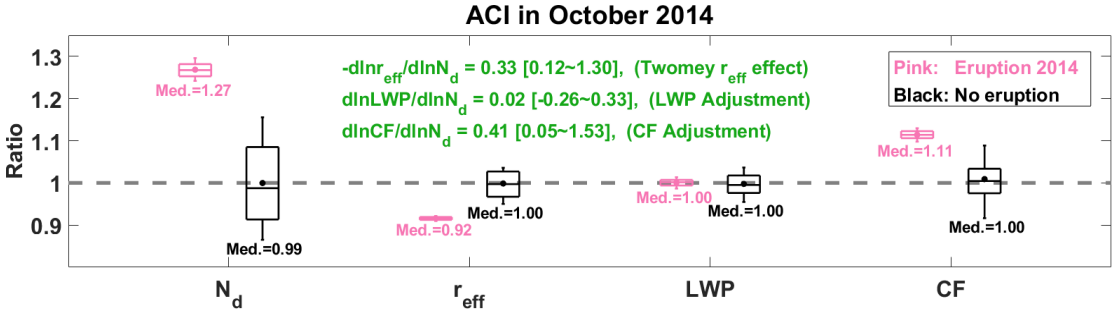

Fig. 3 | Responses of cloud properties to the volcanic aerosol-perturbation in October 2014. The aerosol-cloud interactions (ACI) signals of responses are indicated as the ratios between MODIS (Aqua and Terra) observations and machine-learning predictions, i.e., Ratio = MODIS divided by ML-MODIS. Uncertainties of non-perturbed baseline references are estimated using a Monte Carlo method and are shown in black (see Methods, based on non-volcanic October datasets spanning 2001-2020). The variability of the cloud responses to the Holuhraun volcanic aerosol perturbation are shown in pink. The boxplots show 10th, 25th, median (Med.), 75th and 90th percentiles with the mean value indicated by a dot. The susceptibilities of r_{eff}, LWP and CF to changes in N_d are given in a green colour, median [90% confidence interval]. Area (in units of km^2) weighted averaging is used to calculate average cloud properties over the geographical region (Fig. 2), in order to estimate an unbiased large-scale response signal. Therefore, the ratios shown here are slightly different from the slopes shown in Fig. 1, in which area-weighted averaging is not applied.

Extended Data Figures.

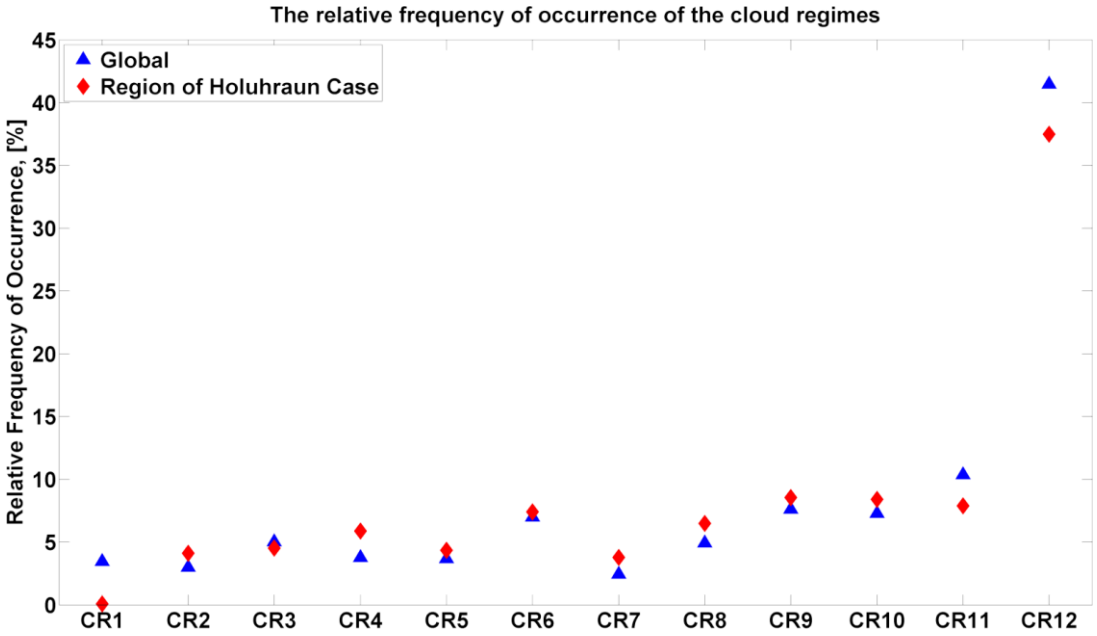

Extended Data Fig. 1 | Relative frequency of occurrence (RFO) of cloud regimes. The RFO values of the region studied here in September-October 2014 are given in red diamonds, data sourced from Malavelle et al.[15]. The RFO values during 2002-2014 globally are given in blue triangles, data sourced from Oreopoulos et al.[40]. CR6-CR11 are liquid-dominated cloud regimes, and the others are ice-dominated cloud regimes. The details of each cloud regime are given in the above references accordingly.

686

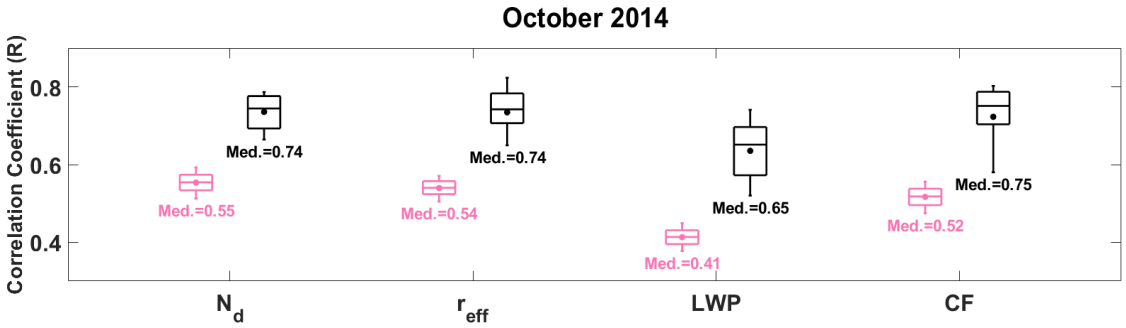

Extended Data Fig. 2 | Correlation coefficient between machine-learning predictions and MODIS observations of cloud properties, including liquid cloud droplet number concentration (N_d), liquid droplet effective radius (r_{eff}), liquid water path (LWP) and liquid cloud fraction (CF). The Monte Carlo results of ML-MODIS validation against MODIS observations without volcanic aerosol-perturbation are given in black. The variations of comparisons with volcanic aerosol-perturbation in October 2014 are given in pink. The boxplot shows 10th, 25th, median (Med.), 75th and 90th percentiles with the mean value indicated by a dot.

687

688

689

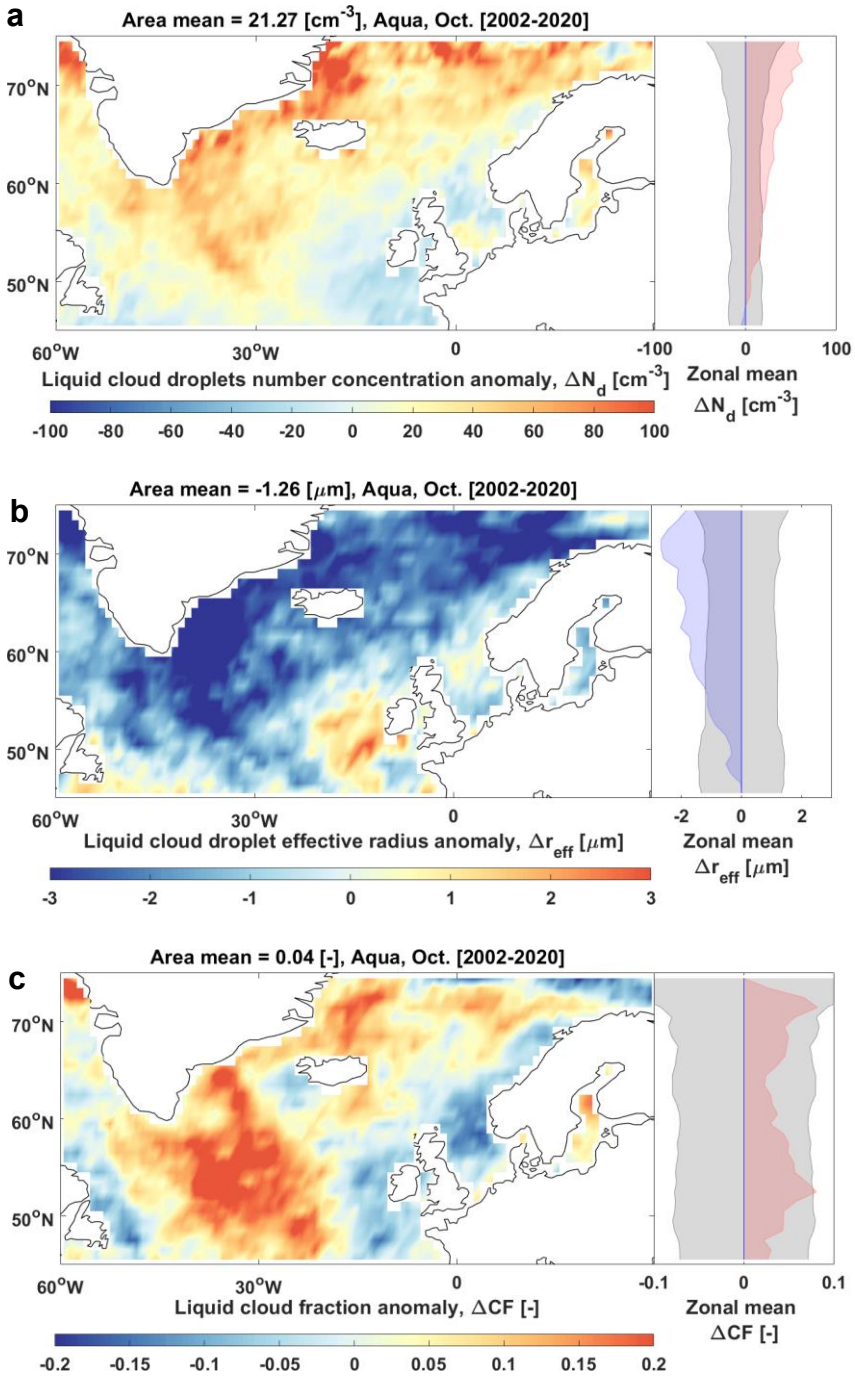

Extended Data Fig. 3 | Anomalies in MODIS-Aqua cloud properties for October 2014. The spatial distributions and zonal means of anomalies in N_d, r_{eff} and CF are shown in the panels **a-c**. Anomalies correspond to the deviation from the 2002-2020 climatology (excluding the 2014 eruption year). The positive anomalies are shown in red and negative ones in blue. The standard deviation is shown by the grey shading.

690

691

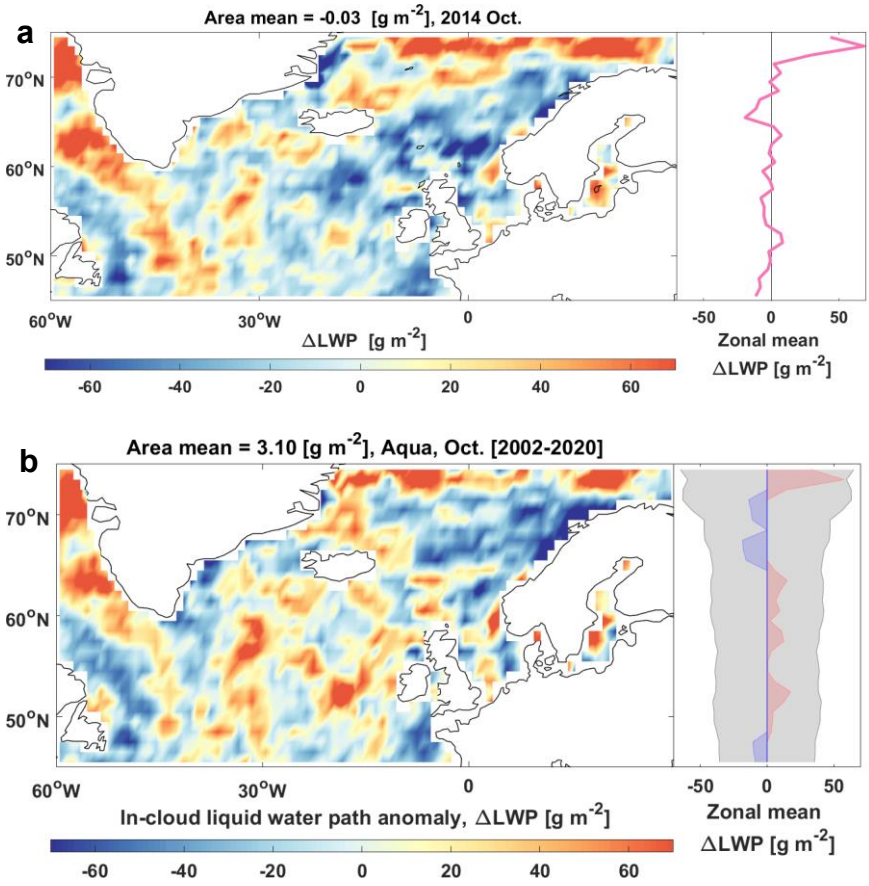

Extended Data Fig. 4 | Change (a) and anomaly (b) in liquid water path (LWP). a) Similar to Fig. 2, changes are detected using machine-learning; **b)** similar to Extended Data Fig. 3, anomaly corresponds to the deviation from 2002-2020 climatology.

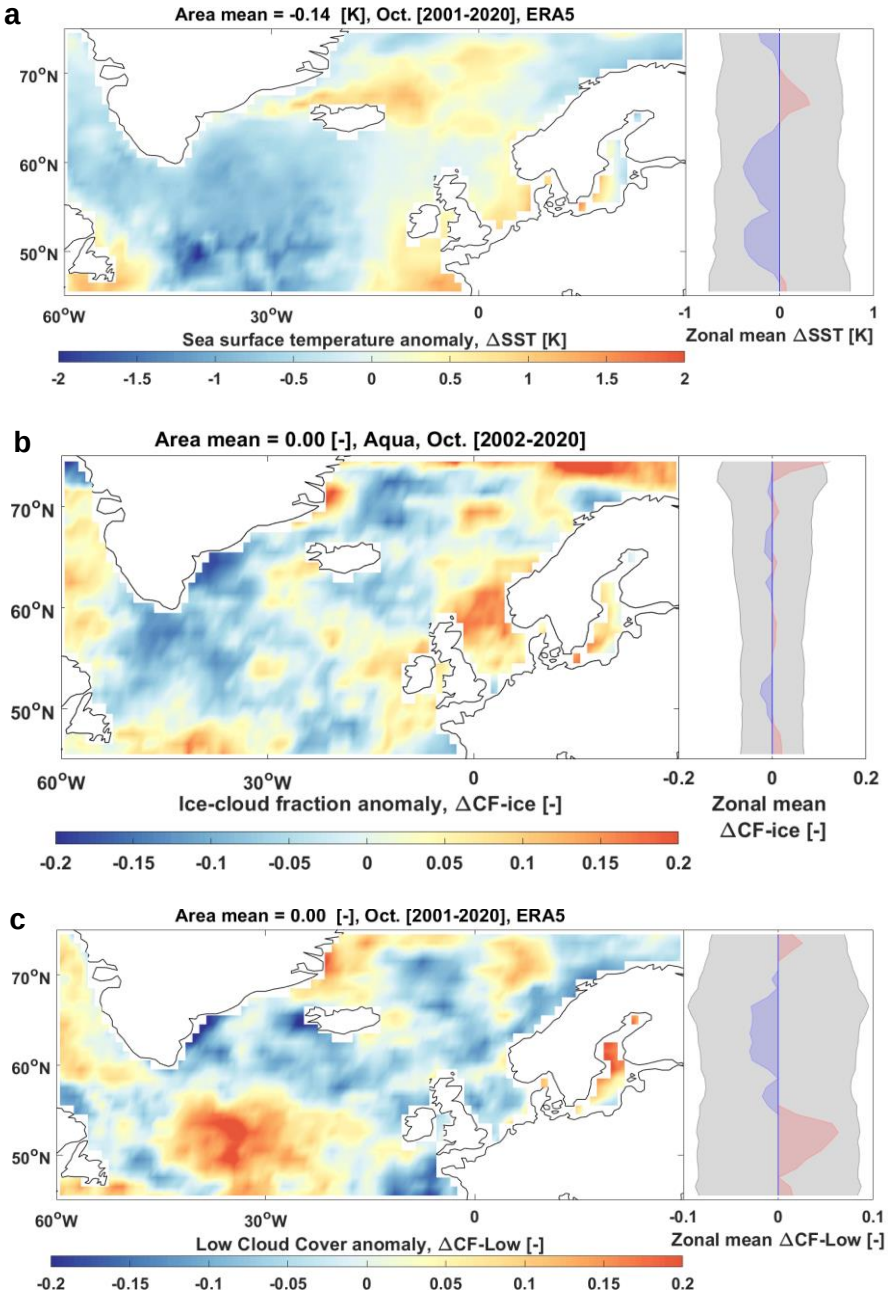

Extended Data Fig. 5 | Similar to Extended Data Fig. 3, but show anomaly in sea-surface temperature **(a),** anomaly in ice-cloud fraction in October 2014 **(b),** and climatological anomaly of low-level cloud cover in October 2014 using ERA5 reanalysis **(c)**.

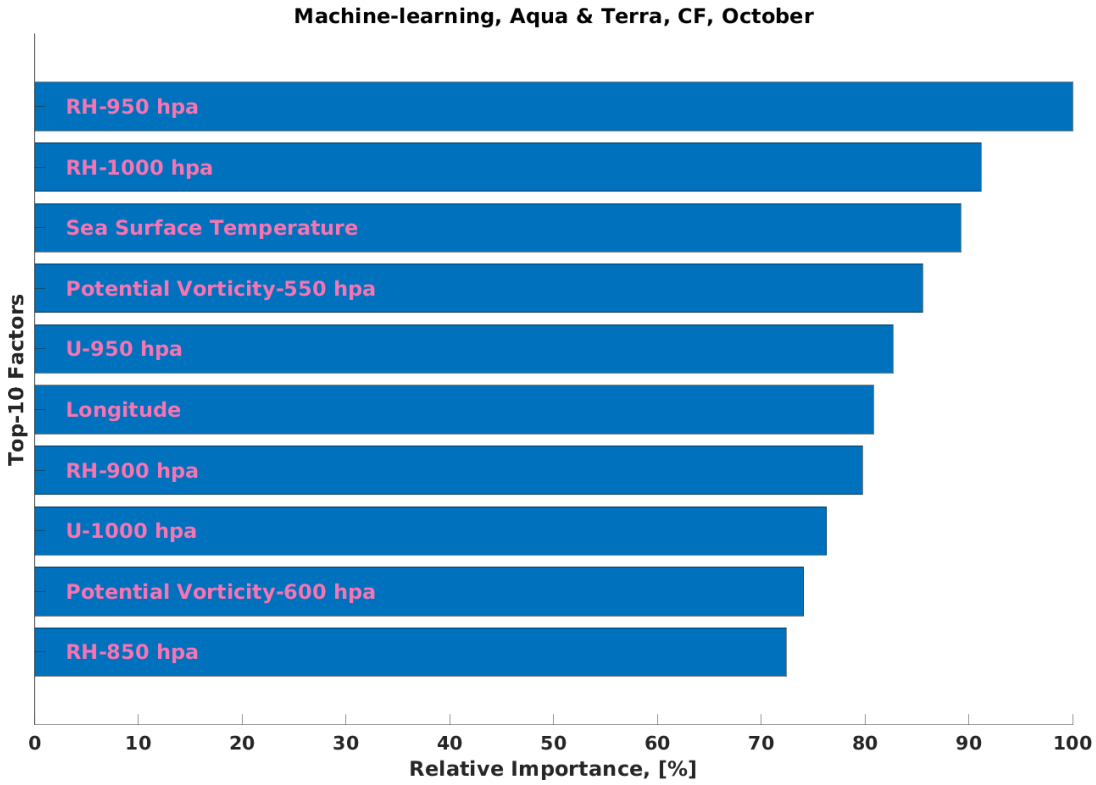

Extended Data Fig. 6 | The top-10 most important features for machine-learning to predict unperturbed liquid cloud fraction in October. The feature importance is normalized with the maximum as 100%. The value of these features in 2014 are entirely within the variation range of machine-learning training dataset, see Extended Data Fig. 10.

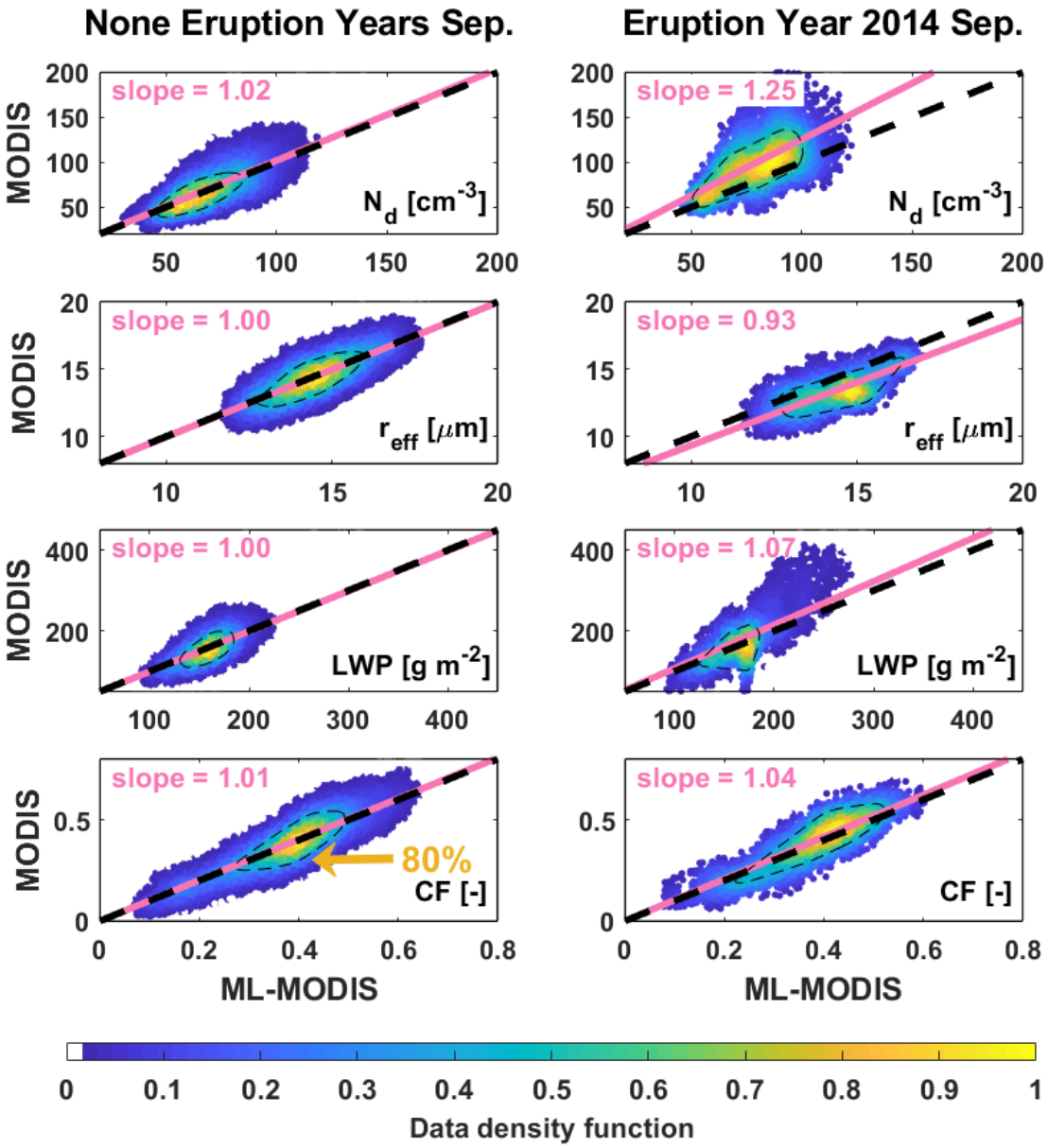

Extended Data Fig. 7 | Similar to Fig. 1, but show results in September 2014.

a

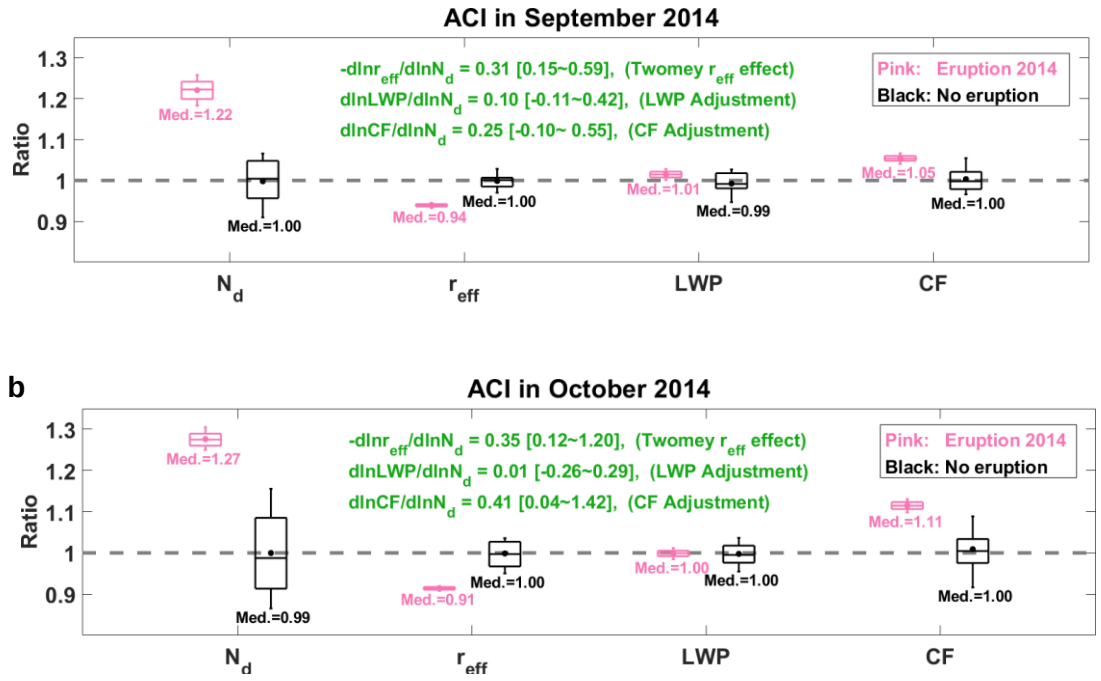

Extended Data Fig. 8 | Similar to Fig. 3. Panel a shows results in September 2014**. Panel b** shows results in October 2014 but excluding the regions where the cold anomalous SSTs were outside the variation range at the same location.

731

732

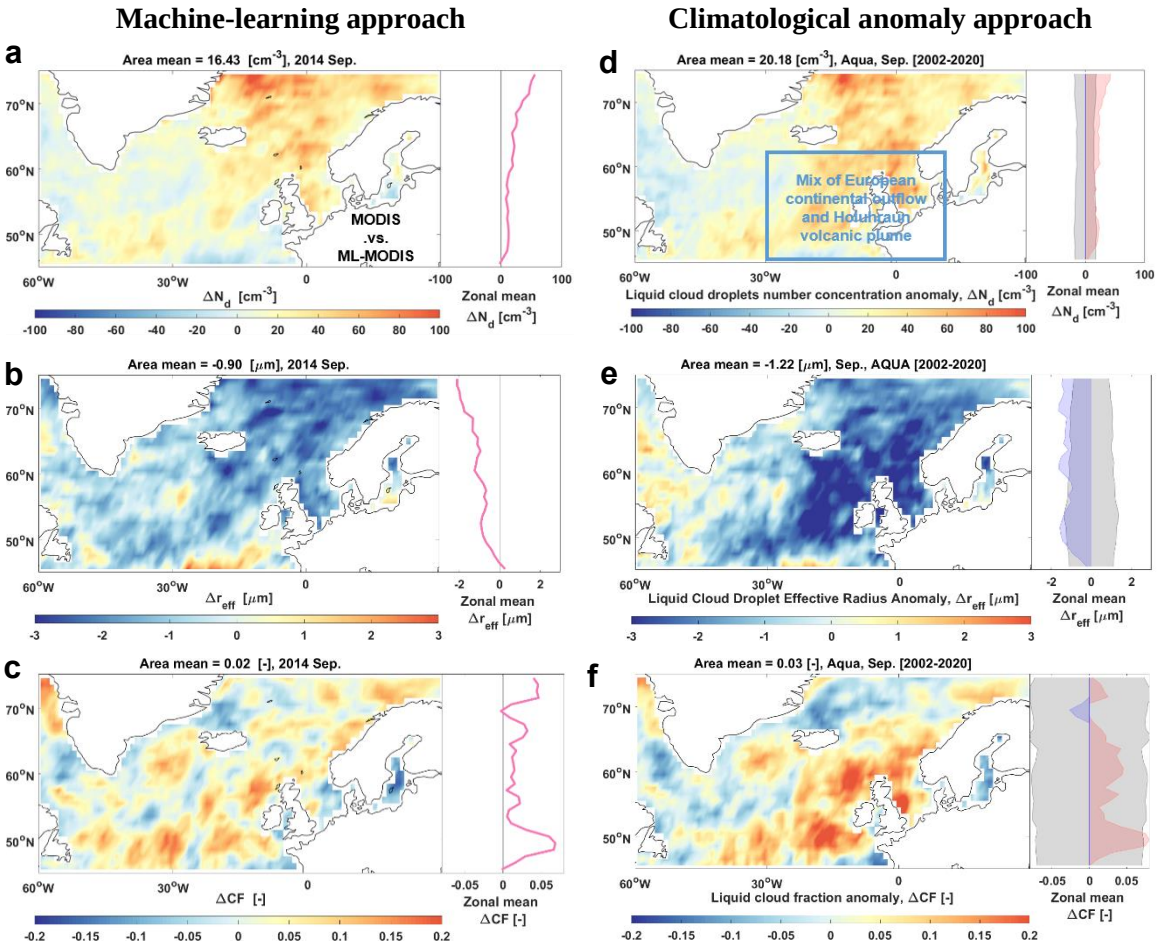

Extended Data Fig. 9 | Cloud responses to Holuhraun volcanic aerosol in September 2014. Left panels **a-c (similar to Fig. 2 but for September 2014)** show cloud responses to volcanic aerosol using machine-learning (ML) approach. Right panels **d-f (similar to Extended Data Fig. 3 but for September 2014)** show anomalies in cloud properties.

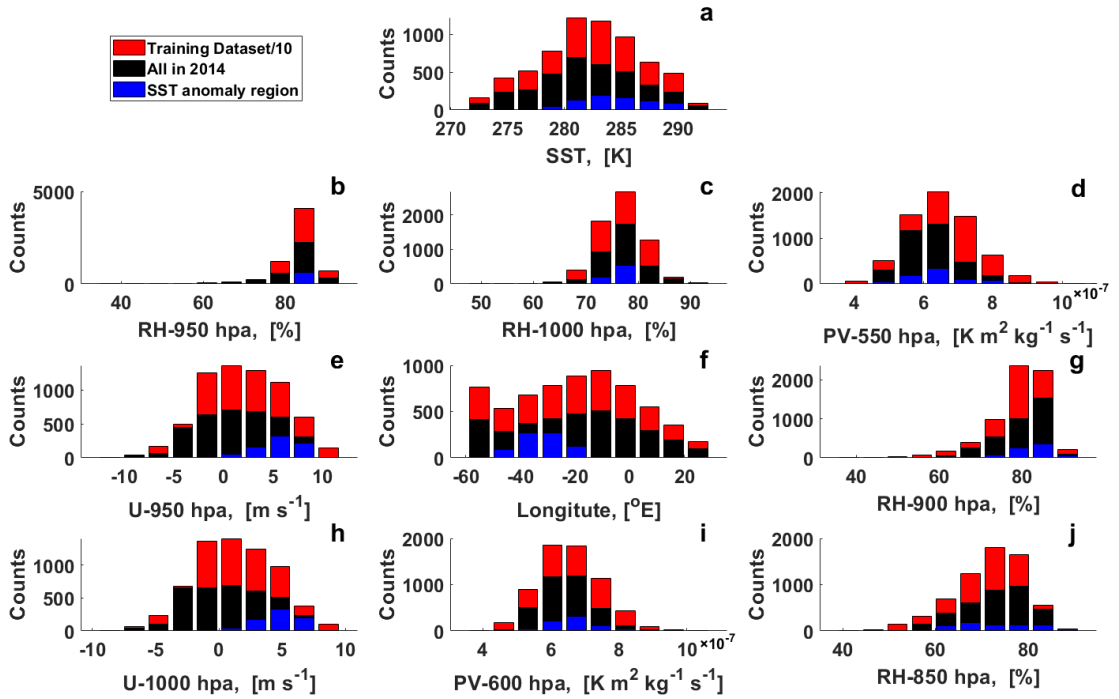

Extended Data Fig. 10 | Probability distribution of the top-10 most important features, as shown in Extended Data Fig. 6. Red bars indicate the counts (scaled by 0.1 to fit the display range) of the training data in each bin, which covers the entire variability range of black and blue bars; black bars indicate the data counts from the entire studied region in October 2014; and blue bars indicate the counts from the SST anomaly region only. Note that the counts per longitude are different, because we only consider data over the oceans.